

Tunable microfluidic standing air bubbles and its application in acoustic microstreaming

Cite as: Biomicrofluidics 13, 034114 (2019); doi: 10.1063/1.5086920

Submitted: 25 December 2018 · Accepted: 14 May 2019 ·

Published Online: 6 June 2019



View Online



Export Citation



CrossMark

Jixiao Liu,^{1,2} Bowen Li,^{1,2} Tong Zhu,^{1,2} Yidi Zhou,^{1,2} Shanshan Li,^{1,2} Shijie Guo,^{1,2,3} and Tiejun Li^{1,2,a}

AFFILIATIONS

¹School of Mechanical Engineering, Hebei University of Technology, Tianjin 300132, China

²Hebei Key Laboratory of Smart Sensing and Human-Robot Interaction, Hebei University of Technology, Tianjin 300132, China

³State Key Laboratory of Reliability and Intelligence of Electrical Equipment, Hebei University of Technology, Tianjin 300132, China

^aAuthor to whom correspondence should be addressed: li_tiejun@hebut.edu.cn

ABSTRACT

Microbubbles are often used in chemistry, biophysics, and medicine. Properly controlled microbubbles have been proved beneficial for various applications by previous scientific endeavors. However, there is still a plenty of room for further development of efficient microbubble handling methods. Here, this paper introduces a tunable, stable, and robust microbubble interface handling mechanism, named as microfluidic standing air bubbles (μ SABs), by studying the multiphysical phenomena behind the gas–liquid interface formation and variation. A basic μ SAB system consists specially structured fluidic channels, pneumatic channels, and selectively permeable porous barriers between them. The μ SABs originate inside the crevice structures on the fluidic channel walls in a repeatable and robust manner. The volumetric variation of the μ SAB is a multiphysical phenomenon that dominated by the air diffusion between the pneumatic channel and the bubble. Theoretical analysis and experimental data illustrate the coupling processes of the repeatable and linear μ SAB volumetric variation when operated under common handling conditions (control pneumatic pressure: -90 kPa to 200 kPa). Furthermore, an adjustable acoustic microstreaming is demonstrated as an application using the alterable μ SAB gas–liquid interface. Derived equations and microscopic observations elucidate the mechanism of the continuous and linear regulation of the acoustic microstreaming using varying μ SAB gas–liquid interfaces. The μ SAB system provides a new tool to handle the flexible and controllable gas–liquid interfaces in a repeatable and robust manner, which makes it a promising candidate for innovative biochemical, biophysical, and medical applications.

Published under license by AIP Publishing. <https://doi.org/10.1063/1.5086920>

INTRODUCTION

After decades of development, microfluidics is still keen to find the killer-applications in the fields of life science, medicine, biophysics, biochemistry, and so on, by enriching the knowledge and technology libraries.^{1,2} Yet, there are still a plenty of essential issues to be solved for the further development of practical products and tools with high-levels of robustness, repeatability, and accuracy.

Microbubbles are often observed and further utilized in microsystems. The microscale bubbles could behave as efficient tools if under proper deployment. Varieties of microbubble formation and control techniques have been developed^{3–11} and utilized in different applications.^{12–21} For other cases, some unwanted microbubbles are accused as one of the sources of performance deterioration, and various bubble removal strategies have been developed.^{22–28}

Unlike the segmented flow or the bubble clusters, the air bubble generated on the microchannel walls or surfaces have

attracted much attention.^{29–31} These microbubbles could function individually or in group, to regulate the microscale flow,^{14,16,32,33} to manipulate the microparticles and cells,^{34–40} and so on. Although efforts have been done in various aspects, there is still a lot of room for further studies of reliable and robust microbubble control methods.^{11,41}

Here, this paper reports an integrated system to generate and to control the robust and functional microbubbles in microfluidic devices, named as the microfluidic standing air bubble (μ SAB) system. A typical μ SAB system consists of crevice structures on the fluidic channel walls, proximal pneumatic channels, and selectively permeable porous barriers between them, as illustrated in Fig. 1. The μ SABs initially take shape in the crevices during the liquid flow and they firmly attach to the channel walls during operations.^{29,30} The size and the geometry of the microbubbles are controlled by the air diffusion between the proximal pneumatic

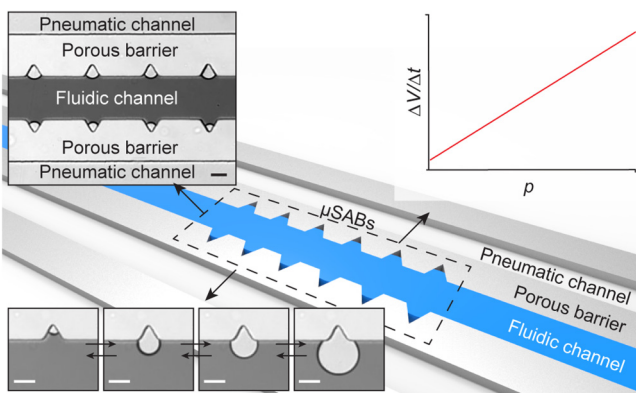


FIG. 1. The microfluidic standing air bubble system. A typical μ SAB system consists of crevice structures on the fluidic channel walls, proximal pneumatic channels and permeable porous barriers. Insets demonstrate the structure schematics (top-left), the control linearity (top-right), and the repeatable bubble variations (bottom-left). Scale bars represent $100\ \mu\text{m}$.

channels and bubble boundaries that is ultimately maneuvered by the pneumatic pressure.²² Although the crevice structure for bubble nucleation has been studied and utilized, the μ SAB system in this report provides significantly improved handling capability and robustness by integrating the control mechanism. The μ SAB(s) can be manipulated individually or in group through single or multiple pneumatic control signal(s). Also, they can provide extra

controllability and stability since the signal disturbance are filtered through the air mass transfer processes, comparing with the syringe pump driven microbubbles.^{15,42} Multiphysical phenomena of the μ SAB formation and volumetric variation are studied with theoretical and experimental approaches.

As an application of the μ SAB system, the adjustable bubble-based acoustic microstreaming phenomenon is demonstrated with theoretical derivations and experimental tests. In addition to the previous approaches, the μ SAB-based system can continuously regulate the microstreaming pattern with good linearity and controllability, by simply tuning the pneumatic pressure. We anticipate that this elegant and functional microbubble system could provide useful tools and methods to the application fields such as life science, medicine, biophysics, and biochemistry.

MICROFLUIDIC STANDING AIR BUBBLE FORMATION

The crevice model of air bubble formation was introduced in 1944 and then have been widely studied.^{29–31} The crevices with small inner angles on microchannels would lead to small gas-pocket formation, as demonstrated in Fig. 2. Based on this physical phenomenon, the μ SAB system introduces proximal pneumatic channels to achieve effective control over the generated microbubbles. The authors have used similar channel structures for fluidic actuation and bubble elimination in previous studies.^{22,23}

In the microfluidic standing air bubble system, the microscale crevices are fabricated on the channel walls to initiate the bubbles, as shown in Fig. 2(a). When the dynamic contact angle between the liquid and the channel walls [α in Fig. 2(b)] is larger than the

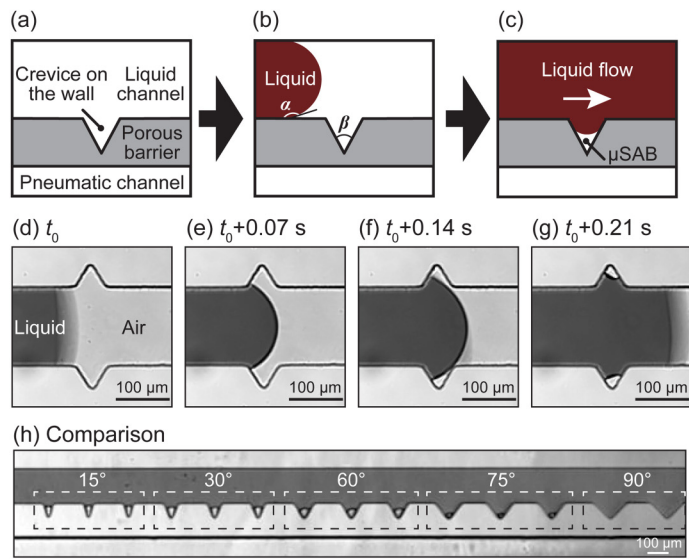


FIG. 2. Microfluidic standing air bubble formation. (a)–(c) The crevice model of microbubble formation. (d)–(g) The microscopic observation of the bubble formation process. The advancing contact angle between the liquid and the channel wall was close to 90° and smaller than 100° . The crevice structures in the tests are designed as equilateral triangles with $75\ \mu\text{m}$ on each side. The fluidic channel depth is $30\ \mu\text{m}$, and the channel width is $150\ \mu\text{m}$. (h) Comparison of bubble formation between crevices with different inner angles. The contact angle between the liquid and the channel wall in the demonstrated experiment is about 90° . (i) The statistic illustration of the bubble formation in different crevice structures. About 20 bubbles have been measured for each condition under same in-flow and pneumatic pressure ($0.5\ \mu\text{l}/\text{min}$ and $20\ \text{kPa}$).

crevice inner angle [β in Fig. 2(b)], the liquid is unable to fill all the space inside the crevices when flowing by, as demonstrated in Figs. 2(a)–2(c). There will be air remained in the crevices to form small bubbles. Figures 2(d)–2(g) are the top view of the μ SAB formation process under microscopic observation. As in Fig. 2(h), conditions of crevice angles between 15° and 120° were experimentally tested and compared with aqueous solutions, which further validated the principle (see more in the [supplementary material](#) for further details). In the experiment, the liquid was syringe-pumped into the serpentine microchannel with a flow rate of $0.5 \mu\text{l}/\text{min}$. At the same time, a positive pneumatic pressure ($\sim 20 \text{ kPa}$) was applied into the pneumatic control channel to balance the liquid pressure.

As illustrated in Fig. 2(i), the bubble formation have been repeated and characterized in crevice structures with different dimensions and inner angles. The plotted data demonstrated that the uniformity of the formed μ SABs is not the same under different structural conditions. The microbubbles formed with larger volume (such as crevices with 30° and 45° in the middle) owns better uniformity based on the plotted data. The largest value of the relative standard deviation (RSD) of the microbubble formation volume is $\sim 15.7\%$ when the crevice inner angle is 15° . The data cannot cover all of the crevice structures and dimensions; nevertheless, it could prove that the formation process is reproducible and robust.

It is commonly believed that the static contact angle between normally made polydimethylsiloxane (PDMS) and water is around 105° , but it varies due to the liquid solution used, aging of material, environmental conditions, fabrications, and operation protocols.⁴³ In this study, the advancing contact angle between the flowing liquid (a mixture of DI water and blue inkjet printer ink, 5:1 in volume) and PDMS-made microchannel surface was in the range of 90° to 110° (based on microscopic pictures, see more in the [supplementary material](#)). It is reasonable since all the experimental procedures followed standard protocols. Combining the previous statements, the threshold angle value of the crevices is considered as 90° for the following section of this report.

Still, the PDMS microchannel surfaces are sensitive to environmental conditions and handling protocols, and it could turn to be either hydrophilic or hydrophobic, or varying between them. However, it will not affect the μ SAB formation process if the crevice angles are far away from the swing range of advancing contact angle. Hence, the testing devices are designed to array 60° crevices on the fluidic channel walls to generate and to control the μ SABs. Most of the previous acoustic microstreaming studies used rectangular cavities inside the channel walls. The triangular crevice structures with 60° inner angles could improve the uniformity of the bubble formation and the robustness of the bubble volumetric variation, as demonstrated below. (See more in the [supplementary material](#).)

MICROFLUIDIC STANDING AIR BUBBLE VOLUMETRIC VARIATION AND CHARACTERIZATION

The PDMS material is highly permeable to air and some other gases, while it prevents the trespassing of aqueous solutions through the material.⁴⁴ The μ SAB system takes advantage of this unique material property, building a barrier between the fluidic channel and the pneumatic channel, to transfer air between the

channels to control the bubble volume. Theoretical and experimental analysis are illustrated in Eqs. (1)–(4), Figs. 3 and 4.

The μ SAB volumetric variation is a multiphysical process that couples interfacial air mass transfer, liquid flow mechanics, and liquid– μ SAB surface tension/pressure balancing, as shown in Figs. 3(a) and 3(b). The pressure inside the μ SAB influences the liquid– μ SAB interface geometry and the air diffusion that further reacts at the μ SAB variation. The liquid– μ SAB interface defines the geometry of the air bubble in liquid and the pressure difference between the liquid and the bubble. The fluid flow influences the bubble shape, the bubble attachment to the fluidic channel wall and the pressure balancing surrounding the bubble, through the liquid pressure and shear exerted on the μ SAB. More important, these physical processes are always coupled to coinfluence the μ SAB variation and hardly analyzed individually.

Theories

Mathematical models are developed to theoretically understand the multiphysical principles during the μ SAB variation process. Considering the time during μ SAB variation, the process could be analyzed as a quasistatic model, hence the coupling multiphysical model could be described by the following equations.

Pressure balancing

The surface tension/pressure balancing surrounding the μ SAB is described as

$$p_b(t) = p_{\text{liq}} + 2\gamma \cos \theta \left[\frac{1}{h} + \frac{1}{r(t)} \right], \quad (1)$$

where $p_b(t)$ is the pressure inside the μ SAB (pascal), p_{liq} is the liquid pressure surrounding the μ SAB (pascal), γ is the surface tension of the liquid (newton per meter), θ is the static contact angle between the liquid and the PDMS (radian), h is the channel height (meter), and $r(t)$ is the equivalent radius of the μ SAB–liquid surface (meter).

The experimental observations (Fig. 2) indicated that the minimal radius/curvature of the μ SABs when they generated in the crevices was about $27 \mu\text{m}$. Still, in all of the tested microfluidic devices, the μ SABs located in the middle of the total length of the microchannels. Hence, based on the experimental data, the Poiseuille flow equation and Eq. (1), the pressure difference between the pneumatic channel and the μ SAB was calculated and plotted in Figs. 3(c) and 3(d). In the calculations, the channel dimensions were the same as the tested devices ($30 \mu\text{m}$ in width, $150 \mu\text{m}$ in height, 21.7 mm in length, the μ SABs were in the middle of the microchannel). The figures indicate that the pressure differences Δp between the proximal pneumatic channel and the μ SAB are majorly dependent on the fluid flow status. However, if under the same flow rate, the pressure difference Δp could be seen as a constant value during the μ SAB volumetric changes.

Bubble volumetric variation

The air mass transfer is the driving force behind all of the seen and unseen physical processes. As mentioned above, when the microbubbles grow and shrink, the pressure inside the μ SABs is

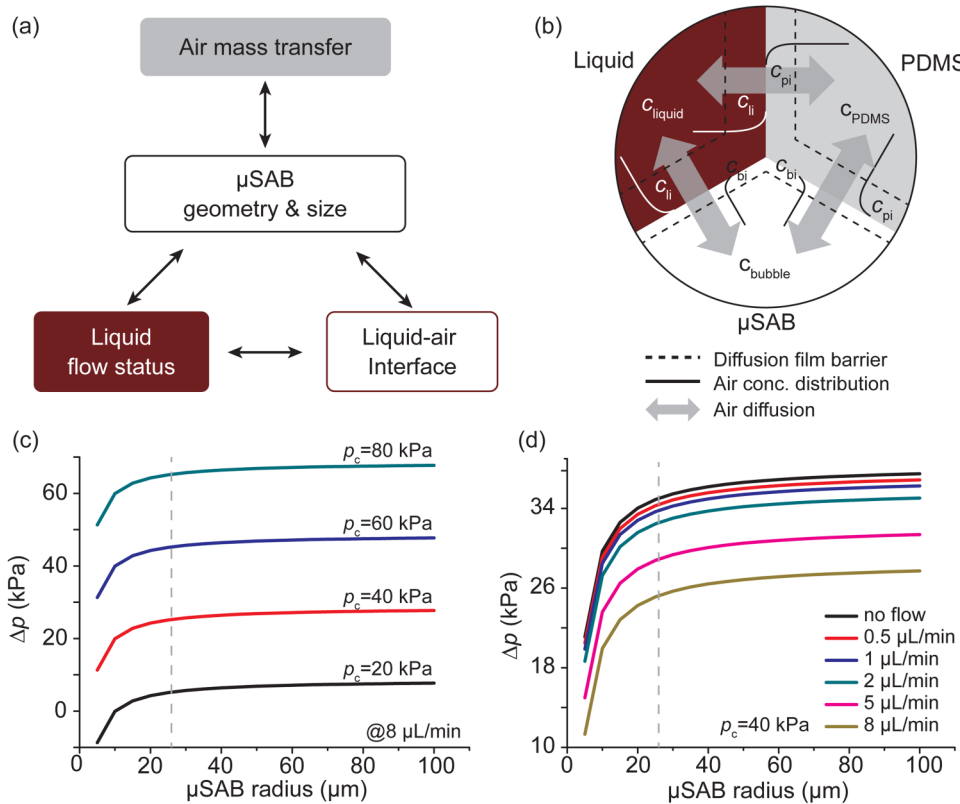


FIG. 3. Multiphysical coupling of the μSAB variation. (a) The μSAB status is dependent on multiple physical processes. (b) The air diffusion among liquid, PDMS, and μSAB could be described with two-film theories of interfacial mass transfer. (c) The pressure difference between the proximal pneumatic channel and the μSAB (Δp) under different pneumatic control pressures. (d) The pressure difference between the proximal pneumatic channel and the μSAB (Δp) under different liquid flow velocities. Plots are based on the calculation results from simulation data. The microchannel dimensions are the same in the tested devices: 30 μm in width, 150 μm in height, 21.7 mm in length, the μSABs are in the middle of the microchannel.

believed as quasistatic. Further, based on Henry's law and two-film theory in the liquid–gas mass transfer, the air concentration on the μSAB side of PDMS barrier is also seen as quasistatic during theoretical analysis for simplification, as illustrated in Fig. 3(b). Similar studies and issues have been described by Salari *et al.*¹¹

To estimate the μSAB variation process, two moments in bubble variation are taken, initial time and t time. Based on the ideal gas law, the variation rate between these two moments could be written as

$$R_V(t) = \frac{V_t - V_0}{t} = RT \frac{\Delta n}{tp_{bt}} - RT \frac{n_0 \Delta p_b}{tp_{b0} p_{bt}}, \quad (2)$$

where $R_V(t)$ is the average rate of the μSAB volumetric variation during the liquid flow ($\text{m}^3 \text{s}^{-1}$); V_t is the μSAB volume in time t (cubic meters); V_0 is the μSAB volume in the initial state (cubic meters); n_t and n_0 are amount of air in the μSAB in time t and initial state (moles); p_{bt} and p_{b0} are the air pressure within μSAB (pascal); R is the gas constant, $R = 8.314 \text{ J K}^{-1} \text{ mol}^{-1}$; T is the temperature (kelvin); Δn is the variation of air amount in bubble (moles); Δp_b is the pressure difference in the μSAB between time t_0 and t (pascal).

Moreover, in Eq. (2),

$$\frac{\Delta n}{tp_t} = \frac{\pi h k_{pa}}{2RT} \frac{\int_0^t r(\lambda) (RT c_{pdms}(\lambda) - sp_b(\lambda)) d\lambda}{tp_t}, \quad (3)$$

where h is the height of the microchannel (meter); k_{pa} is the overall mass transfer constant through the PDMS-μSAB interface (meter per second); $c_{pdms}(t)$ is the air concentration in equilibrium PDMS bulk phase at the PDMS-μSAB interface (not the concentration on the channel wall) (mol m^{-3}); s is the air solubility in PDMS (dimensionless). Besides, the value of $\Delta p_b / p_0 p_t$ is very small since the variation of the Δp_b is ignorable comparing with the value of $(p_0 p_t)$, hence the term $n_0 \Delta p_b / tp_0 p_t$ is negligible compared with the first term on the right side of Eq. (2). Further, it infers a linear relationship between Δn and the μSAB variation rate based on Eqs. (2) and (3).

In Eq. (3), the transient air concentration variation within PDMS walls $c_{pdms}(t)$ could be further written as⁴⁵

$$c_{pdms}(t) = \frac{2}{l} \sum_{n=1}^{\infty} \sin\left(\frac{n\pi z}{l}\right) e^{-\frac{Dn^2\pi^2 t}{l^2}} \left[\int_0^l c(z') \sin\frac{n\pi z'}{l} dz' + \frac{nD\pi}{l} \int_0^t e^{\frac{Dn^2\pi^2 t}{l^2}} \left\{ s \cdot p_b(t) - (-1)^n c_2 \right\} d\lambda \right], \quad (4)$$

where l is the thickness of the PDMS barrier on which concentration gradient place (meter); z is the distance from the fluidic channel wall in the PDMS barrier (meter); $c(z)$ is the concentration distribution in PDMS in the initial state for each moment; c_2 is the concentration in atmosphere (mol m^{-3}); and D is the diffusion coefficient of air in PDMS ($\text{m}^2 \text{s}^{-1}$). This equation is to describe the

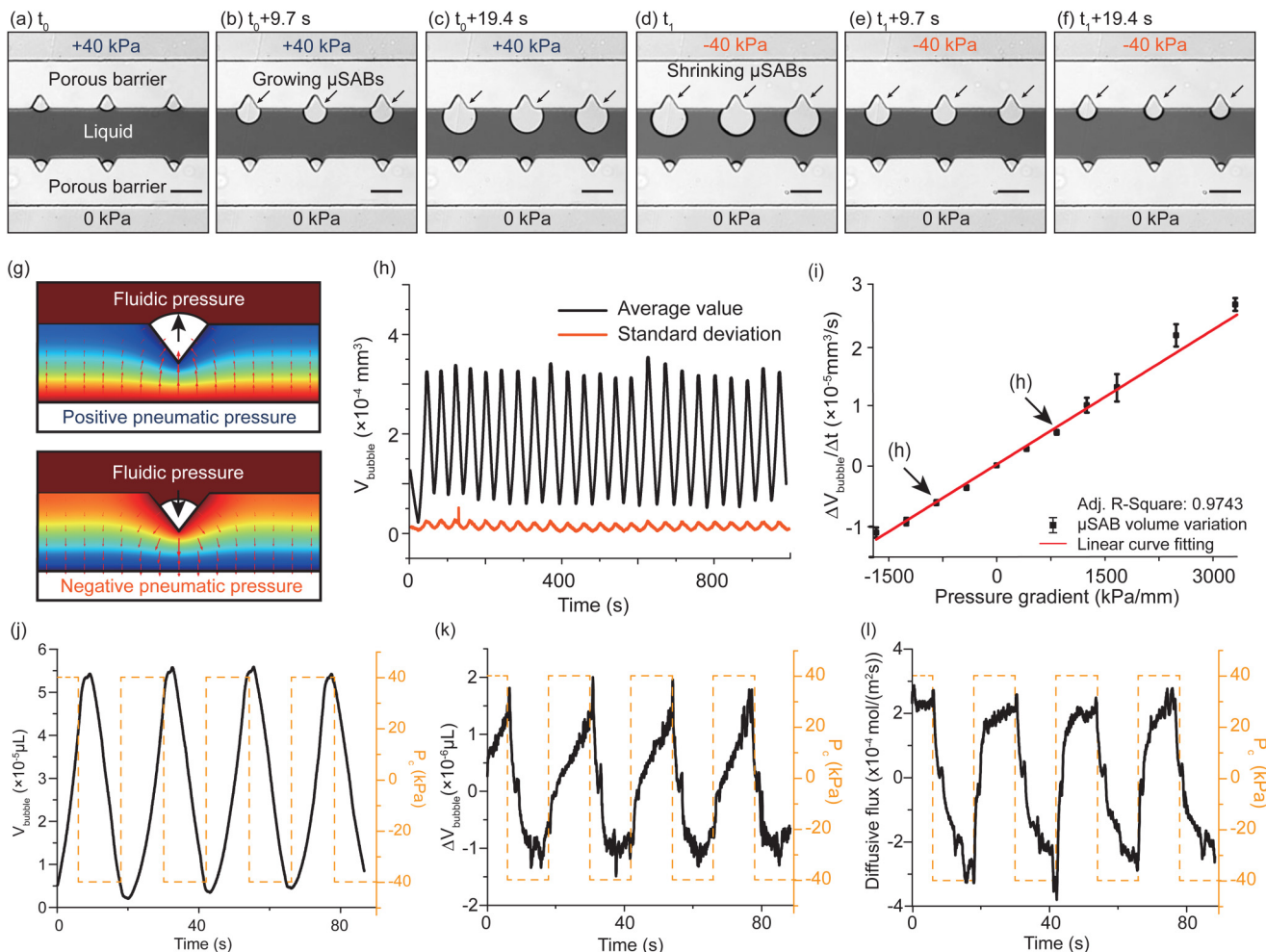


FIG. 4. Microfluidic standing air bubble volumetric variation characterization. (a)–(f) Observation of μSAB volumetric variation under ± 40 kPa cycle. (g) Schematic illustrations of the μSAB growth/shrinkage under positive/negative pressure. (h) Volumetric variation of μSAB under ± 60 kPa cycles for more than 1000 s. Twelve bubbles are controlled at the same time. (i) Experimental data of the relationship between average μSAB volumetric variation rate (volume difference/time period) and pressure gradient (pressure difference/barrier thickness) in growth and shrinkage cycles. The curve fitting (red line) indicates a good linearity in the demonstrated range, and the adjusted R^2 is 0.9743. (j) Experimental data of the μSAB volumetric variation under ± 40 kPa pneumatic control pressure cycles. (k) Experimental data of the transient μSAB volumetric change under pneumatic pressure cycles. (l) Calculated data based on experiments to characterize the air mass transfer process during bubble growth/shrinkage. The calculations were based on the ideal gas law, the bubble pressure and the volume were estimated based on the experimental video.

air mass transfer in a transient state when the first Fick's law is not applicable.

Based on the derived theories and previous studies,¹¹ the experimental characterizations of the μSAB volumetric variation are demonstrated in Fig. 4. In the tested devices, the crevice structures were built in pairs to see the comparison during the bubble variation. When a positive pressure was employed into the pneumatic control channel, it created air pressure/concentration gradient across the porous PDMS barrier, leading to an instant air mass transfer from the pneumatic channel into the formed μSABs. The inward-diffusing air inflated the bubble and changed the geometrical shape under the balancing of surrounding pressure, as shown in Figs. 4(a)–4(c).

On the side without positive pressure, these inactive μSABs only had slight and negligible changes, compared with the active μSABs across the fluidic channel. The reason behind was that the solubility and permeability of air in aqueous solution were much lower than those in the PDMS material (more than an order smaller),⁴⁶ so the air diffused through the aqueous solution to reach the inactive μSABs could hardly vary the bubble. As in Figs. 4(d)–4(f), when the pressure in the pneumatic channel was switched to negative (vacuum), the air mass transfer direction was inverted, as the air started to diffuse out from the μSABs into the pneumatic channel across the porous barrier. Similarly, the inactive μSABs across the fluidic channel were hardly influenced.

Further experimental studies were performed to explain the physical processes behind the observed phenomena, as demonstrated in Figs. 4(h)–4(l). Figure 4(h) is the data from the bubble variation repeatability tests. There were 12 bubbles in the channels and they were manually controlled by the ± 60 kPa pneumatic pressure cycles. The volumetric variation process was measured in ImageJ software. The dark lines are the average volume of the 12 μ SABs, and the orange lines are the calculated standard deviations. The variation process could last for hours if without being disturbed. It indicates superior variation uniformity among the μ SABs, well-behaved variation repeatability and robustness during the growth/shrinkage cycles. Figure 4(i) characterizes the μ SAB volume variation under different pneumatic pressures. Calculation and curve fitting were implemented based on experimental data. In the figure, the μ SAB volume variation rate (averaged for each growth/shrink cycles) is plotted vs the calculated pressure gradient (the pressure differences across the PDMS barriers divided by the thickness of the barrier), under the basic structure design. The fitted curve (the red line) illustrates a linear trend between the average μ SAB volume variation rate and the pressure gradient across the barrier (R^2 is 0.9743). It implies the fact that the air mass transfer intensity into or out of μ SAB, which powers and dominates the bubble variation, is in proportion to the pressure gradient. The illustrated data were measured in no-flow/slow flow conditions (0–2 μ l/min in a 30 μ m high, 150 μ m wide microchannels). Under these conditions, the flow-induced shear force affected the μ SAB shape geometry in a negligible way. When no/small shear stress exerted on the liquid-air interface, most of the observed μ SAB would grow into a symmetric and spherical shape. While liquid flew by the μ SAB at relatively larger velocities, the shear stress would be hardly ignored since it pushed the bubbles into the downstream direction of the fluidic channel, which influenced the air diffusion flux and the pressure/surface tension balancing situation. Further, after the μ SAB diameter exceeded 2/3 of the fluidic channel width or the bubble-liquid interface overflow of the crevice boundaries, most of the bubble variation trends were lack of uniformity, so those circumstances were not considered in the reported characterizations either.

Figure 4(j) demonstrates a single μ SAB volumetric variation process based on the experimental data. Similar to Fig. 4(h), the growth and shrinkage processes of μ SAB are also linear based on the depicted curves. The reason is that the μ SAB volume is proportional to the air amount inside the bubble when the pressure is constant based on the ideal gas law. While the μ SAB pressure during the growth/shrinkage could be seen as quasistatic processes; hence, the bubble volume variation and the total amount of air diffusion are both demonstrated as linear processes. The measured μ SAB variation data demonstrate lags and small fluctuations right after the pressure switches between positive/negative, which is further explained in Figs. 4(k) and 4(l). The direction of the mass transfer in the porous PDMS took time to reverse when the “opposite” control pneumatic pressure was applied. As shown, after the pneumatic pressure was switched, the diffusion kept the same direction in the following seconds. It resulted in the lags and fluctuations in the volumetric variation. Figure 4(l) plots the time-dependent diffusive flux as a nonlinear process, based on the experimental data from Figs. 4(j) to 4(k). The inward air diffusive flux during the bubble growth kept increasing before the pneumatic control pressure was

switched to negative. It indicates that the concentration gradient across the PDMS barrier has not reached equilibrium status before the pneumatic pressure being switched, and the air diffusion that dominated the bubble variation was always a dynamic process.

The theoretical and experimental analysis of the μ SAB volumetric variation could help understand the coupling physics behind the microbubble growth and shrinkage, at the same time of validating that the μ SABs in the microfluidic channels own good controllability, robustness, and repeatability. It will further benefit various applications that require flexible and variable gas–liquid interfaces.

CONTINUOUS VARIATION OF ACOUSTIC MICROSTREAMING BASED ON μ SABS

By adjusting the acoustic source parameters, the bubble-based microstreaming could be functional to manipulate microparticles, cells, and organisms.^{36,39,40,47–49} Based on the characterization of the μ SABs, it was found that by directly controlling the μ SAB dimension and morphology, the continuous and linear microstreaming pattern adjustment could be achieved. This following section illustrates that how the variable μ SABs influence the acoustic microstreaming pattern based on theoretical and experimental approaches.

Theories

The major influencing forces on the particle during the acoustic microstreaming are the radiation force due to the acoustic energy and the drag force due to the particle movement. The radiation force on a particle of volume V_p and density ρ_p in the proximity of a bubble that is pulsating close to resonance is described by²⁹

$$F_{\text{rad}} = -\frac{3V_p(\rho_p - \rho_0)\rho_0\omega^2 R_{\text{eo}}^2 R_o^4}{2\rho_p + \rho_0} \frac{1}{r^5}, \quad (5)$$

where the F_{rad} is the radiation force on the particle from the acoustic energy (newton), V_p is the volume of the particle (cubic meter), ρ_p is the density of the particle (kilogram per cubic meter), ρ_0 is the equilibrium density of liquid (kilogram per meter), ω is the resonance circular frequency of the bubble, $\omega = 2\pi f$ (radian per second), R_{eo} is the radial displacement amplitude of wall of the bubble (meter), R_o is the equilibrium radius of the oscillating bubble (meter), and r is the distance from the bubble interface to the particle position (meter).

Further, R_{eo} in Eq. (5) could be described as

$$R_{\text{eo}} = \frac{P_A}{R_o \rho_o} \frac{1}{\sqrt{(\omega_0^2 - \omega^2)^2 + (2\beta_{\text{tot}}\omega)^2}}, \quad (6)$$

where P_A is the acoustic pressure amplitude (pascal), β_{tot} is the total resistive constant leading to damping, ω_0 is the resonance circular frequency of the bubble, $\omega_0 = 2\pi f_0$, f_0 is the resonance frequency of the oscillating bubble (hertz).

Hence, the radiation force F_{rad} could be further written as

$$F_{\text{rad}} = -\frac{4\pi a^3(\rho_p - \rho_0)}{2\rho_p + \rho_0} \frac{\rho_0 \omega^2 P_A^2 R_o^2}{r^5 \rho_0^2 [(\omega_0^2 - \omega^2)^2 + (2\beta_{\text{tot}}\omega)^2]}. \quad (7)$$

At the same time, the oscillating bubble induces a streaming flow in proximity, and the particles inside the flow experience

drag forces

$$F_{\text{drg}} = -6\pi\mu av_p, \quad (8)$$

where F_{drg} is the drag force on a particle in the liquid flow (newton), a is the radius of the particle (meter), μ is the liquid viscosity (pascal second), and v_p is the relative velocity between the particle and the surrounding liquid (meter per second).

The physical phenomenon of particle movement in the liquid near the oscillating bubble is complexed and coeffected by multiple factors. However, the ratio of between the magnitude of radiation force and the drag force could reflect the relative importance within the microstreaming pattern.

Hence, the ratio between magnitudes of the radiation force and the drag could be further written as

$$\frac{F_{\text{rad}}}{F_{\text{drg}}} = \frac{2a^2 P_A^2 R_o^2 (\rho_p - \rho_0)}{3\mu v_p r^5 \rho_0 (2\rho_p + \rho_0) \left[\frac{(\omega_0^2 - \omega^2)^2}{\omega^2} + (2\beta_{\text{tot}})^2 \right]}. \quad (9)$$

If $\omega \approx \omega_0$, then

$$\frac{F_{\text{rad}}}{F_{\text{drg}}} = \frac{a^2 (\rho_p - \rho_0)}{6\mu \rho_0 (2\rho_p + \rho_0)} \frac{P_A^2 R_o^2}{\beta_{\text{tot}}^2} \frac{1}{v_p r^5}. \quad (10)$$

In the equation, the particle relative velocity v_p is a function of multiple variables, such as position, acoustic energy density, and so on. Following the similar approximation,^{50,51} the nonoscillatory streaming has a limiting value, given by

$$v_{p,\text{max}} = \frac{CP_A^2}{\omega R_o^4 r^5}, \quad (11)$$

where the C is a constant that depends on the device structure and acoustic source. Then, Eq. (10) could be simplified into

$$\left(\frac{F_{\text{rad}}}{F_{\text{drg}}} \right)_{\text{limit}} = \frac{a^2 (\rho_p - \rho_0)}{6\mu \rho_0 (2\rho_p + \rho_0)} \frac{\omega}{C \beta_{\text{tot}}^2 R_o^2}. \quad (12)$$

In the equation above, two major variables, ω and R_o , influence the microstreaming. The other parameters are dependent on particle properties and liquid properties. Also, $(F_{\text{rad}}/F_{\text{drg}})_{\text{limit}}$ are different with $(F_{\text{rad}}/F_{\text{drg}})$, since $(F_{\text{rad}}/F_{\text{drg}})_{\text{limit}}$ describes the limit status when the particle velocity is at its largest values and it is irrelevant to the particle positions. Similar forms of this equation have been reported.^{49,50,52} However, it is found that the derived equations in this report could directly describe the influence of the bubble volumetric variation on the acoustic microstreaming pattern.

Although the oscillating bubble-based acoustic microstreaming has been widely studied, it still requires further works to study how the continuous bubble variation influences the streaming patterns. The μ SAB system provides a new access to study the variable acoustic microstreaming with the flexible and controllable bubble interfaces, as shown in Fig. 5. The 5 μm (in diameter) polystyrene microspheres (Beisile, Tianjin, China, 1:100 v/v diluted from 2.5% w/v solution) circulated in the vortex close to the bubble under acoustic excitation, and the experiments indicated that the vortex circulation range expanded during the μ SAB shrinkage.

Equation (12) describes that the value of $(F_{\text{rad}}/F_{\text{drg}})_{\text{limit}}$ is proportional to the reciprocal of the μ SAB area, when other handling conditions are not changed. As shown in Fig. 5, the area of the microstreaming was proportional to the invert of the area of the spherical section of the μ SABs. The area of the streaming vortex was related to the total energy of the circulating particles,

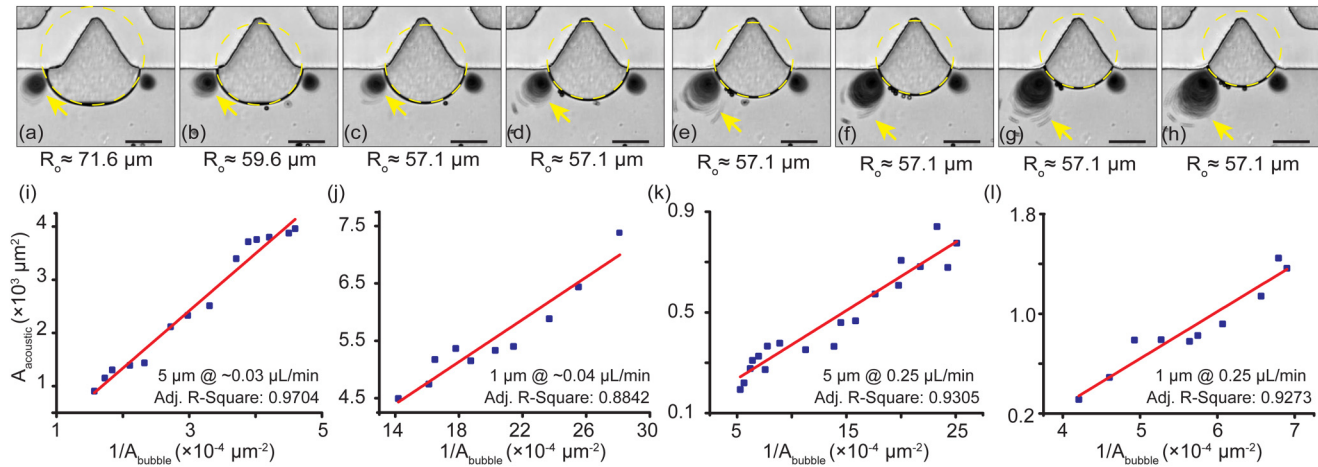


FIG. 5. Particle acoustic microstreaming pattern variation during μ SAB growth and shrinkage. (a)–(h) The acoustic microstreaming pattern variation is related to the microbubble volumetric variation. Scale bars are 50 μm . (i)–(l) Experimental data indicate linear relations between the reciprocal of the μ SAB volume. All of the four demonstrated conditions were operated with 10 V_{pp} voltage at 70 kHz. The area of the microstreaming and the microbubble area were measured with ImageJ software. The phenomenon was observed repeatedly under different conditions, such as polystyrene (PS) microsphere diameter and liquid flow rate. Other parameters, such as polystyrene microsphere numbers in liquid and μ SAB numbers, have been considered and believed not influential to the plotted linearity. All the data were the averaged values based on three measurements. Liquid flow rate was manually measured with ImageJ software (from NIH).

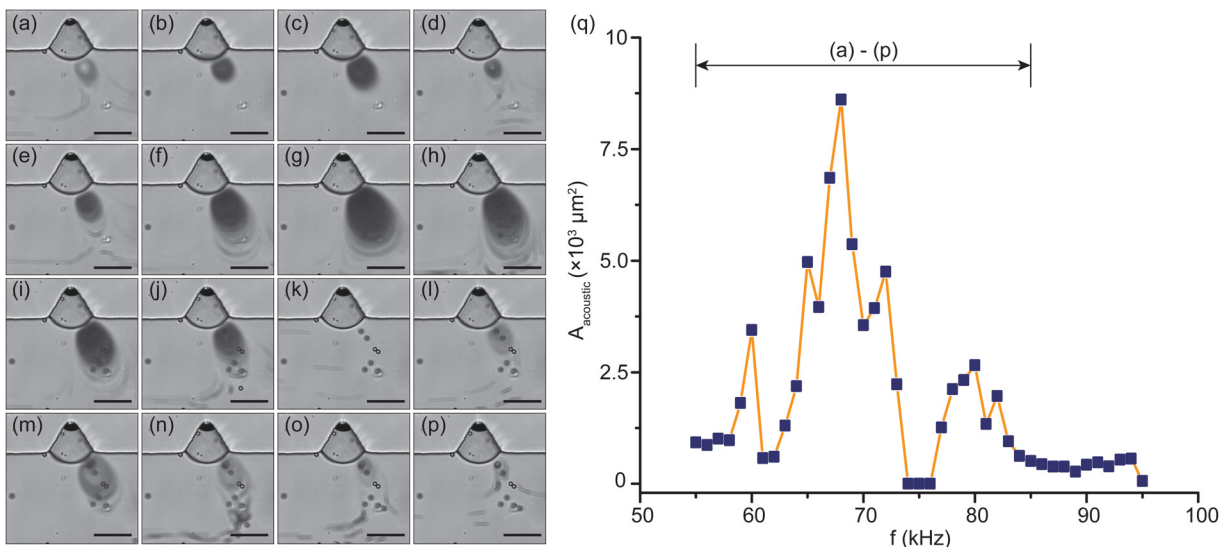


FIG. 6. Particle acoustic microstreaming pattern variation under driving voltage frequency change. (a)–(p) Acoustic microstreaming pattern variation with driving voltage frequencies from 55 kHz to 85 kHz with intervals of 2 kHz. Scale bars are 50 μm . (g) The area of the microstreaming vortex vs driving voltage frequency. No obvious trend was observed based on the data. The data are the average values based on three separate measurements.

since larger kinetic energy the particles owned, the larger area they can reach. Figures 5(a)–5(h) are the image sequences when the μ SAB shrinks, and Figs. 5(i)–5(l) are the plots between the invert of the area of the spherical section of the μ SABs and the area of the particle streaming, under four different conditions. Although the microbubble-based acoustofluidics is complex, the plotted data demonstrated strong linearity between the μ SAB dimension (inverted value) and the microstreaming pattern.

As stated above, the drive voltage frequency f (or the circular frequency ω) is also a crucial parameter in Eqs. (6) and (12). Tests have been implemented to see how the drive voltage frequency influences the microstreaming pattern. As demonstrated in the figures, the driving voltage frequency cannot continuously control the microstreaming pattern of microspheres since the relationship between the vortex pattern and the driving voltage frequency is not with apparent relation, similarly to the previous studies.⁴⁷ The reason is that the change of the drive voltage frequency would vary the oscillation mode of the bubble interface and multiple peaks are the results of these oscillation mode shifts.

As shown in Figs. 5 and 6, there were two flow microstreaming vortexes observed near the bubble, and the size of the left vortex was larger than the right one. The reason of choosing the asymmetric streaming pattern in the figure is to avoid the interferences between the nearby streaming patterns. Besides, there were continuous microspheres flowing from the upstream microchannel to minimize the possibility of observation errors. In the demonstrated test, the microstreaming was oscillated by an acoustic wave from the piezoelectric transducer that was driven by the AC voltage signal (from 1 V_{pp} to 10 V_{pp}, from 55 kHz to 120 kHz, by Tektronix AFG1022 and TEGAM Model 2035 as the signal generator and voltage amplifier). The liquid flow rate is 0–1 $\mu\text{l}/\text{min}$. The pneumatic control pressure of the μ SAB is ± 40 kPa.

The liquid flow and particle trace under acoustic energy are the results of coupled multiphysics, and they are dependent on various conditions and structural parameters. Here in this paper, we use variable μ SABs to study the phenomena for better control of the microstreaming. The variation of the particle microstreaming pattern is found to be linear to the reciprocal of the μ SAB volume, and it provides a new insight into the theoretical studies of the acoustic microstreaming, at the same time of a better control method in the potential applications.

CONCLUSIONS

This paper majorly studies an innovative approach of controlling and utilizing standing microbubble interfaces in microfluidic devices. The study developed a control mechanism to manipulate the standing air bubble volumetric variation, with theoretical studies and experimental characterizations. The μ SABs form in the crevice structures on the microfluidic channel walls when liquid flow by, and the dimension of the μ SABs are controlled under the control pressure in the proximal pneumatic channel. Theoretical and experimental studies validated that the μ SAB formation and variation owns good robustness and repeatability. Furthermore, experimental data demonstrated a linear relationship between the μ SAB volumetric variation and the pneumatic pressure gradient, and the linear character will ensure the bubble controllability with enhanced robustness and simplified bubble handling methods.

Based on the μ SAB system, an acoustic microstreaming continuous variation phenomenon was studied. Since the μ SAB system could handle a single microbubble or microbubble arrays with ease by the pneumatic pressure, it provides new perspectives to utilize the acoustic microstreaming effects. A theoretical model was developed to describe the relationship between the ratio of $F_{\text{rad}}/F_{\text{drg}}$ and

μ SAB dimension, and experimental observation validated the assumed linear relationship between the microstreaming pattern and the μ SAB dimension. Compare with the drive voltage frequency, the μ SAB volumetric variation could be more direct and useful for acoustic microstreaming adjustment.

The μ SAB system is a combinational concept of microbubble formation and control, and it is further a promising platform that could benefit various applications. The controllable and robustness liquid-gas interfaces make the μ SABs a strong candidate for numerous applications, such as precise flow regulation, accurate micromanipulation, high-throughput gas-liquid chemical synthesis, and other novel biochemistry and biophysical applications.

SUPPLEMENTARY MATERIAL

See the [supplementary material](#) for the preliminary application demonstrations of the μ SAB system, details of bubble characterizations, and protocols of experiments.

ACKNOWLEDGMENTS

This work is financially supported by the National Natural Science Foundation of China (NNSFC) (Grant Nos. 51605136 and 51505123), the China Postdoctoral Science Foundation (No. 2016M600180), and the Natural Science Foundation of Hebei Province (Nos. E2017202248 and E2015202194). The authors would like to thank Professor Luke P. Lee from the UC Berkeley for discussions and support.

REFERENCES

- ¹E. K. Sackmann, A. L. Fulton, and D. J. Beebe, *Nature* **507**(7491), 181–189 (2014).
- ²G. M. Whitesides, *Nature* **442**(7101), 368–373 (2006).
- ³P. Garstecki, M. J. Fuerstman, H. A. Stone, and G. M. Whitesides, *Lab Chip* **6**(3), 437–446 (2006).
- ⁴T. Fu, Y. Ma, D. Funfschilling, and H. Z. Li, *Chem. Eng. Sci.* **64**(10), 2392–2400 (2009).
- ⁵C.-L. Zhang, Y.-Q. Wang, Y. Gong, Y. Wu, G.-D. Peng, and Y.-J. Rao, *J. Lightwave Technol.* **36**(12), 2492–2498 (2018).
- ⁶B. M. Borkent, S. Gekle, A. Prosperetti, and D. Lohse, *Phys Fluids* **21**(10), 102003 (2009).
- ⁷J. Zhao and Z. You, *Cytometry A* **93**(2), 222–231 (2018).
- ⁸C.-M. Cheng and C.-H. Liu, *J. Microelectromech. Syst.* **15**(2), 296–307 (2006).
- ⁹Z. Z. Chong, S. B. Tor, N. H. Loh, T. N. Wong, A. M. Ganan-Calvo, S. H. Tan, and N. T. Nguyen, *Lab Chip* **15**(4), 996–999 (2015).
- ¹⁰Y. Hong, N. Ashgriz, J. Andrews, and H. Parizi, *J. Microelectromech. Syst.* **13**(5), 857–869 (2004).
- ¹¹A. Salari, V. Gnyawali, I. M. Griffiths, R. Karshfian, M. C. Kolios, and S. S. H. Tsai, *Soft Matter* **13**(46), 8796–8806 (2017).
- ¹²M. Lee, E. Y. Lee, D. Lee, and B. J. Park, *Soft Matter* **11**(11), 2067–2079 (2015).
- ¹³C. Walsh, N. Ovenden, E. Stride, and U. Cheema, *Sci. Rep.* **7**(1), 6331 (2017).
- ¹⁴A. Oskooei, M. Abolhasani, and A. Gunther, *Lab Chip* **13**(13), 2519–2527 (2013).
- ¹⁵K. Khoshmanesh, A. Almansouri, H. Albloushi, P. Yi, R. Soffe, and K. Kalantar-Zadeh, *Sci. Rep.* **5**, 9942 (2015).
- ¹⁶Y. Xu, Y. Lv, L. Wang, W. Xing, and J. Cheng, *Biosens. Bioelectron.* **32**(1), 300–304 (2012).
- ¹⁷J. J. M. Cornejo, E. Matsuoka, and H. Daiguji, *Soft Matter* **7**(5), 1897–1902 (2011).
- ¹⁸A. Tomak and H. M. Zareie, *RSC Adv.* **5**(49), 38842–38845 (2015).
- ¹⁹A. Darabi, P. G. Jessop, and M. F. Cunningham, *Chem. Soc. Rev.* **45**(15), 4391–4436 (2016).
- ²⁰Y. Inatsu, T. Kitagawa, N. Nakamura, S. Kawasaki, D. Nei, M. L. Bari, and S. Kawamoto, *Food Sci. Technol. Res.* **17**(6), 479–485 (2011).
- ²¹S. V. Bortkevitch, S. A. Kostrov, N. V. Savitsky and W. O. Wooden, “Method and apparatus for enhanced oil recovery by injection of a micro-dispersed gas-liquid mixture into the oil-bearing formation.” U.S. Patent 7,059,591 (June 13, 2006).
- ²²J. Liu, S. Li, and D. Mitra, *Int. J. Heat Mass Transf.* **91**, 611–618 (2015).
- ²³J. Liu, D. Mitra, J. R. Waldeisen, R. H. Henrikson, Y. Park, S. Li, and L. P. Lee, presented at the 17th International Conference on Miniaturized Systems for Chemistry and Life Sciences, Freiburg, Germany, MicroTAS, 27–31 October 2013.
- ²⁴C. Lochovsky, S. Yasotharan, and A. Gunther, *Lab Chip* **12**(3), 595–601 (2012).
- ²⁵H.-B. Cheng and Y.-W. Lu, *Microfluid. Nanofluid.* **17**(5), 855–862 (2014).
- ²⁶Y. J. Kang, E. Yeom, E. Seo, and S. J. Lee, *Biomicrofluidics* **8**(1), 014102 (2014).
- ²⁷J. Xu, X. Lv, Y. Wei, L. Zhang, R. Li, Y. Deng, and X. Xu, *Sens. Actuators B* **212**, 472–480 (2015).
- ²⁸W. F. Zheng, Z. Wang, W. Zhang, and X. Y. Jiang, *Lab Chip* **10**(21), 2906–2910 (2010).
- ²⁹T. Leighton, *The Acoustic Bubble* (Academic Press, 2012).
- ³⁰A. A. Atchley and A. Prosperetti, *J. Acoust. Soc. Am.* **86**(3), 1065–1084 (1989).
- ³¹E. N. Harvey, A. Whiteley, W. McElroy, D. Pease, and D. Barnes, *J. Cell. Comp. Physiol.* **24**(1), 23–34 (1944).
- ³²H. T. Kim, H. Bae, Z. Zhang, A. Kusimo, and M. Yu, *Biomicrofluidics* **8**(5), 054126 (2014).
- ³³E. Karatay, P. A. Tsai, and R. G. H. Lammertink, *Soft Matter* **9**(46), 11098–11106 (2013).
- ³⁴N. Garg, T. M. Westerhof, V. Liu, R. Liu, E. L. Nelson, and A. P. Lee, *Microsyst. Nanoeng.* **4**, 17085 (2018).
- ³⁵D. Ahmed, H. S. Muddana, M. Lu, J. B. French, A. Ozcelik, Y. Fang, P. J. Butler, S. J. Benkovic, A. Manz, and T. J. Huang, *Anal. Chem.* **86**(23), 11803–11810 (2014).
- ³⁶D. Ahmed, A. Ozcelik, N. Bojanala, N. Nama, A. Upadhyay, Y. Chen, W. Hanna-Rose, and T. J. Huang, *Nat. Commun.* **7**, 11085 (2016).
- ³⁷C. Wang, S. V. Jalikop, and S. Hilgenfeldt, *Biomicrofluidics* **6**(1), 012801–012811 (2012).
- ³⁸S. Yazdi and A. M. Ardekani, *Biomicrofluidics* **6**(4), 044114 (2012).
- ³⁹J. Collis, R. Manasseh, P. Liovic, P. Tho, A. Ooi, K. Petkovic-Duran, and Y. Zhu, *Ultrasonics* **50**(2), 273–279 (2010).
- ⁴⁰H. Chen, Y. Gao, K. Petkovic, S. Yan, M. Best, Y. Du, and Y. Zhu, *Microfluid. Nanofluid.* **21**(3), 30 (2017).
- ⁴¹A. Volk, M. Rossi, C. J. Kahler, S. Hilgenfeldt, and A. Marin, *Lab Chip* **15**(24), 4607–4613 (2015).
- ⁴²J. Xu and D. Attinger, *J. Micromech. Microeng.* **17**(3), 609 (2007).
- ⁴³K. Haubert, T. Drier, and D. Beebe, *Lab Chip* **6**(12), 1548–1549 (2006).
- ⁴⁴L. Xu, H. Lee, D. Jetta, and K. W. Oh, *Lab Chip* **15**(20), 3962–3979 (2015).
- ⁴⁵H. Carslaw and J. Jaeger, *Conduction of Heat in Solids* (Clarendon Press, Oxford, 1959).
- ⁴⁶L. Shui, J. C. Eijkel, and A. van den Berg, *Adv. Colloid Interface Sci.* **133**(1), 35–49 (2007).
- ⁴⁷P. Tho, R. Manasseh, and A. Ooi, *J. Fluid Mech.* **576**, 191–233 (2007).
- ⁴⁸A. Ozcelik, J. Rufo, F. Guo, Y. Gu, P. Li, J. Lata, and T. J. Huang, *Nat. Methods* **15**(12), 1021–1028 (2018).
- ⁴⁹Y. Chen and S. Lee, *Integr. Comp. Biol.* **54**(6), 959–968 (2014).
- ⁵⁰D. L. Miller, *J. Acoust. Soc. Am.* **84**(4), 1378–1387 (1988).
- ⁵¹H. Bruus, *Lab Chip* **12**(6), 1014–1021 (2012).
- ⁵²Y. Xie, D. Ahmed, M. I. Lapsley, M. Lu, S. Li, and T. J. Huang, *J. Lab. Autom.* **19**(2), 137–143 (2014).